Simulation of Coupled Thermal/Hydrological/Mechanical Phenomena in Porous Media

P. H. Winterfeld and **Yu-Shu Wu,** Colorado School of Mines

Summary

For processes such as production from low-permeability reservoirs and storage in subsurface formations, reservoir flow and the reservoir stress field are coupled and affect one another. This paper presents a thermal/hydrological/mechanical (THM) reservoir simulator that is applicable to modeling such processes. The fluid- and heat-flow portion of our simulator is for general multiphase, multicomponent, multiporosity systems. The geomechanical portion consists of an equation for mean stress, derived from linear elastic theory for a thermo-poroelastic system, and equations for stress-tensor components that depend on mean stress and other variables. The integral finite-difference method is used to solve these equations. The mean-stress and reservoir-flow variables are solved implicitly, and the remaining stress-tensor components are solved explicitly. Our simulator is verified by use of analytical solutions for stress- and strain-tensor components and is compared with published results.

Introduction

For processes such as oil and gas production from low-permeability and unconsolidated reservoirs, energy production from geothermal reservoirs, and carbon-dioxide storage in deep saline aquifers, an analysis of fluid and heat flow coupled with rock deformation is advantageous over one of fluid and heat flow alone because reservoir flow and the reservoir stress field affect one another (Rutqvist and Tsang 2002; Chin et al. 2002; Xiong et al. 2013).

To simulate such a THM process, the two sets of equations, the fluid and heat flow and the geomechanics are both solved on a discretized medium. The different ways these two sets of equations can be coupled were described by Settari and Walters (1999) and Tran et al. (2005). Three of these methods are iterative, explicit, and full-coupling. In iterative coupling, the fluid- and heat-flow equations and the geomechanical equations are solved iteratively and sequentially until solutions for both sets converge. Examples of THM processes being simulated with iterative coupling include Chin et al. (2002) and Settari and Mourits (1998). In explicit coupling, one set of equations is solved for first and the other set is solved for next with the updated variables of the previously solved for set. Explicit coupling is a special case of iterative coupling, with only one iteration taken. An example of THM processes being simulated with explicit coupling is Minkoff et al. (1999). In full coupling, both sets of equations are solved simultaneously. Examples of THM processes being simulated with full coupling include Gutierrez and Lewis (1998) and Wan et al. (2003).

A fully coupled THM simulator was presented by Winterfeld and Wu (2014) and Hu et al. (2013). In their approach, the geomechanical equations relating stresses and displacements were combined to yield an equation for mean stress, a primary variable, and volumetric strain, a rock property. The computational cost of fully coupling this geomechanical formulation to the fluid- and heat-flow equations is relatively small because there is only one additional equation and primary variable. However, that formulation is not able to calculate the stress-tensor components and information from these components, such as principal-stress directions that are applicable to predicting rock failure (Jaeger et al. 2007), is lacking.

In this paper, we present a technique to obtain stress-tensor components in the context of this mean-stress geomechanical formulation. We begin by summarizing the mean-stress geomechanical formulation, along with the associated fluid- and heat-flow formulation, and then illustrate the technique for how to obtain stress-tensor components. Four example problems are then used to provide verification of our technique. The first is a comparison of simulation results to the analytical solution for displacement by a uniform load on a semi-infinite elastic medium. The second is a comparison of simulation to the analytical solution for the 2D Mandel-Cryer effect. The third and fourth, a single-phase depletion problem and a simulation of carbon dioxide (CO_2) injection into a depleting gas field, show a comparison of our simulator to published results.

Fluid- and Heat-Flow Formulation

Our simulator's fluid and heat flow formulation is based on the TOUGH2 one (Pruess et al. 1999) for general multiphase, multicomponent, multiporosity systems. Fluid advection is described with a multiphase version of Darcy's law. Heat flow occurs by conduction and convection, the latter including sensible as well as latent heat effects. The description of thermodynamic conditions is based on the assumption of local equilibrium of all phases and rock media. The conservation equations for mass and energy can be written in differential form as

$$\frac{\partial M^k}{\partial t} = \nabla \cdot \mathbf{F}^k + q^k, \quad \ldots\ldots\ldots\ldots\ldots\ldots\ldots\ldots \quad (1)$$

where superscript k refers to a conserved species (mass or energy), M is conserved species per unit volume, q is source or sink per unit volume, and $\mathbf{F}$ is flux. There are N conserved mass components, and energy is denoted by index $N+1$. Mass per unit volume is a sum over phases:

$$M^k = \phi \sum\nolimits_l S_l \rho_l X_l^k, 1 \le k \le N, \quad \ldots\ldots\ldots\ldots\ldots\ldots \quad (2)$$

where ϕ is porosity, subscript l refers to a phase, S is phase saturation, ρ is phase mass density, and X is phase mass fraction. Energy per unit volume accounts for internal energy in rock and fluid and is the following:

$$M^{N+1} = (1-\phi) C_r \rho_r T + \phi \sum\nolimits_l S_l \rho_l U_l, \quad \ldots\ldots\ldots\ldots \quad (3)$$

where ρ_r is rock density, C_r is rock specific heat, and U is phase-specific internal energy.

Advective mass flux is a sum over phases:

$$\mathbf{F}_{\text{adv}}^k = \sum\nolimits_l \mathbf{F}_l X_l^k, 1 \le k \le N, \quad \ldots\ldots\ldots\ldots\ldots\ldots \quad (4)$$

and phase flux $\mathbf{F}_l$ is given by the multiphase version of Darcy's law,

This paper (SPE 173210) was accepted for presentation at the SPE Reservoir Simulation Symposium, Houston, 23–25 February 2015, and revised for publication. Original manuscript received for review 23 March 2015. Revised manuscript received for review 10 September 2015. Paper peer approved 7 October 2015.

$$\mathbf{F}_l = -k\frac{k_{rl}\rho_l}{\mu_l}\left(\nabla P + \nabla P_{c,l} - \rho_l \mathbf{g}\right), \quad \ldots\ldots\ldots\ldots\ldots (5)$$

where k is absolute permeability, k_r is phase relative permeability, μ is phase viscosity, P_c is phase capillary pressure, and $\mathbf{g}$ is the gravity vector. Capillary pressure is relative to a reference phase, which is the gaseous phase. Energy flux includes conductive and convective components:

$$\mathbf{F}^{N+1} = -k_t \nabla T + \sum\nolimits_l h_l \mathbf{F}_l, \quad \ldots\ldots\ldots\ldots\ldots\ldots (6)$$

where k_t is thermal conductivity and h is specific enthalpy.

Mean-Stress Geomechanical Formulation

Our simulator's mean-stress geomechanical formulation is based on the classical theory of elasticity extended to multiporosity nonisothermal media. In the theory of elasticity, the stress/strain behavior of an isothermal elastic material is described by Hooke's law:

$$\boldsymbol{\tau} = 2G\boldsymbol{\varepsilon} + \lambda(tr\boldsymbol{\varepsilon})\mathbf{I}, \quad \ldots\ldots\ldots\ldots\ldots\ldots\ldots\ldots (7)$$

where G is shear modulus and λ is the Lamé parameter. For a thermo-poroelastic medium, a porous medium subject to changes in both temperature and stress, a pore pressure and a temperature term are added to Eq. 7 (McTigue 1986), yielding

$$\boldsymbol{\tau} - \alpha P\mathbf{I} - 3\beta K(T - T_{\text{ref}})\mathbf{I} = 2G\boldsymbol{\varepsilon} + \lambda(tr\boldsymbol{\varepsilon})\mathbf{I}, \quad \ldots\ldots\ldots (8)$$

where α is Biot's coefficient, T_{ref} is reference temperature for a thermally unstrained state, K is bulk modulus, and β is linear thermal-expansion coefficient.

Bai et al. (1993) present a generalization of Hooke's law for a multiporosity medium, a common example of which is the dual-porosity medium consisting of a network of fractures and rock matrix:

$$\boldsymbol{\tau} - \sum\nolimits_j \alpha_j P_j \mathbf{I} = 2G\boldsymbol{\varepsilon} + \lambda(tr\boldsymbol{\varepsilon})\mathbf{I}, \quad \ldots\ldots\ldots\ldots\ldots\ldots (9)$$

where the summation is over multiporosity continua. We obtain Hooke's law for a thermo-multiporoelastic medium by including the temperature term from Eq. 8 in Eq. 9 for each multiporosity continuum, because temperature varies between multiporosity continua. We also weight each temperature term by the porous continuum volume fraction, ω_j, because the bulk modulus and linear thermal-expansion coefficient describe the overall porous medium:

$$\boldsymbol{\tau} - \left\{\sum\nolimits_j [\alpha_j P_j + 3\beta K\omega_j\left(T_j - T_{\text{ref}}\right)]\right\}\mathbf{I} = 2G\boldsymbol{\varepsilon} + \lambda(tr\boldsymbol{\varepsilon})\mathbf{I}. \quad \ldots\ldots\ldots\ldots\ldots\ldots (10)$$

Expressions for the generalized Biot's coefficients, α_j, for a dual-porosity medium were presented by Wilson and Aifantis (1982):

$$\alpha_1 = 1 - \frac{K}{K_*} \quad \ldots\ldots\ldots\ldots\ldots\ldots\ldots\ldots\ldots\ldots (11)$$

and

$$\alpha_2 = \frac{K}{K_*}\left(1 - \frac{K_*}{K_s}\right), \quad \ldots\ldots\ldots\ldots\ldots\ldots\ldots\ldots (12)$$

where K_s is the solid modulus, K_* is the modulus of the porous medium without the fractures, subscript 1 refers to the fractures, and subscript 2 refers to the matrix.

Two other fundamental relations in the theory of linear elasticity are the relation between the strain tensor and the displacement vector $\mathbf{u}$,

$$\boldsymbol{\varepsilon} = \frac{1}{2}(\nabla\mathbf{u} + \nabla\mathbf{u}^t), \quad \ldots\ldots\ldots\ldots\ldots\ldots\ldots\ldots (13)$$

and the static equilibrium equation,

$$\nabla \cdot \boldsymbol{\tau} + \mathbf{F}_b = 0, \quad \ldots\ldots\ldots\ldots\ldots\ldots\ldots\ldots\ldots\ldots (14)$$

where $\mathbf{F}_b$ is the body force. We combine Eqs. 10, 13, and 14 to obtain the thermo-multiporoelastic Navier equation:

$$\nabla\left[\sum\nolimits_j \left(\alpha_j P_j + 3\beta K\omega_j T_j\right)\right] + (\lambda + G)\nabla(\nabla \cdot \mathbf{u}) + G\nabla^2\mathbf{u} + \mathbf{F}_b = 0. \quad \ldots\ldots\ldots\ldots\ldots\ldots\ldots (15)$$

Taking the divergence of Eq. 15 yields

$$\nabla^2\left[\sum\nolimits_j \left(\alpha_j P_j + 3\beta K\omega_j T_j\right)\right] + (\lambda + 2G)\nabla^2(\nabla \cdot \mathbf{u}) + \nabla \cdot \mathbf{F}_b = 0. \quad \ldots\ldots\ldots\ldots\ldots\ldots\ldots (16)$$

The trace of the stress tensor, an invariant, is obtained from Eq. 10 as

$$K\varepsilon_v = \tau_m - \sum\nolimits_j [\alpha_j P_j + 3\beta K\omega_j\left(T_j - T_{\text{ref}}\right)], \quad \ldots\ldots\ldots (17)$$

where τ_m is the mean stress, the average of the normal stress-tensor components, and ε_v is the volumetric strain, the sum of the normal strain components. Finally, combining Eqs. 16 and 17 and noting that the divergence of the displacement vector is the volumetric strain yield an equation relating mean stress, pore pressures, and temperatures (Winterfeld and Wu 2014):

$$\nabla \cdot \left\{\frac{3(1-\upsilon)}{1+\upsilon}\nabla\tau_m + \mathbf{F}_b - \frac{2(1-2\upsilon)}{1+\upsilon} \times \nabla\left[\sum\nolimits_j \left(\alpha_j P_j + 3\beta K\omega_j T_j\right)\right]\right\} = 0, \quad \ldots\ldots\ldots\ldots (18)$$

where υ is Poisson's ratio.

We couple fluid and heat flow to geomechanics by solving Eq. 18 along with the mass and energy conservation equations (Eq. 1) from the fluid and heat flow formulation. Eq. 18 is a momentum conservation equation in terms of mean stress, the primary thermodynamic variable associated with our geomechanical formulation. Volumetric strain is an additional property arising from our geomechanical formulation and is calculated from Eq. 17.

Rock properties, namely porosity and permeability, are correlated to effective stress, a general definition of which was given by Biot and Willis (1957):

$$\tau' = \tau_m - \alpha P. \quad \ldots\ldots\ldots\ldots\ldots\ldots\ldots\ldots\ldots\ldots (19)$$

One such correlation for porosity is based on its definition, the ratio of fluid volume to bulk volume:

$$\phi = 1 - \frac{V_s}{V_0(1 - \varepsilon_v)}, \quad \ldots\ldots\ldots\ldots\ldots\ldots\ldots\ldots (20)$$

where V_s is the solid or grain volume and V_0 is the unstrained bulk volume. Other such correlations for these properties used in our simulator appear in Winterfeld and Wu (2014).

Stress-Tensor Component Formulation

In this section, we derive equations for calculation of the stress-tensor components. Consider the x-component of Eq. 15:

$$\frac{\partial}{\partial x}[h(\mathbf{P}, \mathbf{T})] + (\lambda + G)\frac{\partial}{\partial x}(\nabla \cdot \mathbf{u}) + G\nabla^2 u_x + F_{b,x} = 0, \quad \ldots\ldots\ldots\ldots\ldots\ldots (21)$$

where

$$h(\mathbf{P}, \mathbf{T}) = \sum\nolimits_j [\alpha_j P_j + 3\beta K\omega_j\left(T_j - T_{\text{ref}}\right)]. \quad \ldots\ldots\ldots (22)$$

Differentiating Eq. 21 by x and eliminating strains and displacements in favor of stresses with Eqs. 10, 13, and 17 yield an equation relating the xx-normal stress component, mean stress, pore pressures, and temperatures:

Equation	Associated Primary Variables
Conservation of mass (Eq. 1)	Pressure, $N-1$ mass fractions
Conservation of energy (Eq. 1)	Temperature
Mean stress (Eq. 18)	Mean stress
Normal stresses (Eq. 23)	*xx, yy, zz* normal stresses
Shear stresses (Eq. 24)	*xy, yz, xz* shear stresses

Table 1—Summary of single-porosity version formulation including equations and associated primary variables for N mass components.

$$\frac{\partial^2}{\partial x^2}[h(\mathbf{P},\mathbf{T})]+\frac{3}{2(1+\upsilon)}\frac{\partial^2}{\partial x^2}[\tau_m-h(\mathbf{P},\mathbf{T})]+\frac{1}{2}\nabla^2\left\{\tau_{xx}-h(\mathbf{P},\mathbf{T})-\frac{3\upsilon}{1+\upsilon}[\tau_m-h(\mathbf{P},\mathbf{T})]\right\}+\frac{\partial}{\partial x}F_{b,x}=0. \quad (23)$$

Repeating this procedure for the y- and z-components of Eq. 15 yields similar equations for the yy- and zz-normal stress components:

$$\frac{\partial^2}{\partial y^2}[h(\mathbf{P},\mathbf{T})]+\frac{3}{2(1+\upsilon)}\frac{\partial^2}{\partial y^2}[\tau_m-h(\mathbf{P},\mathbf{T})]+\frac{1}{2}\nabla^2\left\{\tau_{yy}-h(\mathbf{P},\mathbf{T})-\frac{3\upsilon}{1+\upsilon}[\tau_m-h(\mathbf{P},\mathbf{T})]\right\}+\frac{\partial}{\partial y}F_{b,y}=0 \quad (24)$$

$$\frac{\partial^2}{\partial z^2}[h(\mathbf{P},\mathbf{T})]+\frac{3}{2(1+\upsilon)}\frac{\partial^2}{\partial z^2}[\tau_m-h(\mathbf{P},\mathbf{T})]+\frac{1}{2}\nabla^2\left\{\tau_{zz}-h(\mathbf{P},\mathbf{T})-\frac{3\upsilon}{1+\upsilon}[\tau_m-h(\mathbf{P},\mathbf{T})]\right\}+\frac{\partial}{\partial z}F_{b,z}=0. \quad (25)$$

Consider the y-component of Eq. 15:

$$\frac{\partial}{\partial y}[h(\mathbf{P},\mathbf{T})]+(\lambda+G)\frac{\partial}{\partial y}(\nabla\cdot\mathbf{u})+G\nabla^2u_y+F_{b,y}=0. \quad (26)$$

Differentiating Eq. 26 by x, differentiating Eq. 21 by y, averaging the two, and eliminating strains and displacements as before yield an equation relating the xy-shear stress component, mean stress, pore pressures, and temperatures:

$$\frac{\partial^2}{\partial x\partial y}[h(\mathbf{P},\mathbf{T})]+\frac{3}{2(1+\upsilon)}\frac{\partial^2}{\partial x\partial y}[\tau_m-h(\mathbf{P},\mathbf{T})]+\frac{1}{2}\nabla^2\tau_{xy}+\frac{1}{2}\left(\frac{\partial}{\partial x}F_{b,y}+\frac{\partial}{\partial y}F_{b,x}\right)=0. \quad (27)$$

Repeating this procedure for the y- and z-components of Eq. 15 yields an equation for the yz-shear stress component; repeating this procedure for the x- and z-components of Eq. 15 yields an equation for the xz-shear stress component:

$$\frac{\partial^2}{\partial y\partial z}[h(\mathbf{P},\mathbf{T})]+\frac{3}{2(1+\upsilon)}\frac{\partial^2}{\partial y\partial z}[\tau_m-h(\mathbf{P},\mathbf{T})]+\frac{1}{2}\nabla^2\tau_{yz}+\frac{1}{2}\left(\frac{\partial}{\partial y}F_{b,z}+\frac{\partial}{\partial z}F_{b,y}\right)=0 \quad (28)$$

$$\frac{\partial^2}{\partial x\partial z}[h(\mathbf{P},\mathbf{T})]+\frac{3}{2(1+\upsilon)}\frac{\partial^2}{\partial x\partial z}[\tau_m-h(\mathbf{P},\mathbf{T})]+\frac{1}{2}\nabla^2\tau_{xz}+\frac{1}{2}\left(\frac{\partial}{\partial x}F_{b,z}+\frac{\partial}{\partial z}F_{b,x}\right)=0. \quad (29)$$

Eqs. 23 through 25 and 27 through 29 relate each normal or shear-stress component to mean stress, pore pressures, and temperatures, the primary variables of the mean-stress geomechanical formulation.

Discretization and Solution of Simulator Equations

The fluid and heat flow and geomechanical equations are discretized in space with the integral finite-difference method (Narasimhan and Witherspoon 1976). In this method, the simulation domain is subdivided into gridblocks, and those equations are integrated over a gridblock volume, V:

$$\frac{\mathrm{d}}{\mathrm{d}t}\int_V M^k\mathrm{d}V=\int_\Gamma \mathbf{F}^k\cdot\mathbf{n}\mathrm{d}\Gamma+\int_V q^k\mathrm{d}V, \quad (30)$$

where Γ is the gridblock surface. Because geomechanical effects result in gridblock geometry changes, the integrands of Eq. 25 depend on strain. This dependence is formulated as

$$\psi(\varepsilon_\psi)=\psi_0(1-\varepsilon_\psi),\psi=A,D,\text{or } V, \quad (31)$$

where subscript 0 refers to zero strain, A refers to area, D refers to distance, and V refers to volume. Replacing volume integrals with gridblock volume averages and surface integrals with discrete sums over gridblock surface segment averages yields the following discrete form of the simulator equations:

$$[M^k(1-\varepsilon_v)]^{n+1}-[M^k(1-\varepsilon_v)]^n-\frac{\Delta t}{V_0}\left[\sum_j A_0(1-\varepsilon_{A,j})F_j^k+V_0(1-\varepsilon_v)q^k\right]^{n^*}=0, \quad (32)$$

where the summation is over gridblock surface segments, superscript n is timestep, and superscript n^* bracketing the flux and generation terms denotes that those terms are evaluated at the previous timestep (n) or the current one ($n+1$).

The simulator equations and primary variables comprising the single-porosity version of our formulation are summarized in **Table 1.** This system of equations is solved in a sequential manner with the Newton-Raphson method. The Jacobian matrices consist of square sub-matrices that are associated with a gridblock or a connection between two gridblocks. Conservation of mass, energy, and the mean-stress equation are solved simultaneously first. This solution is also performed in the THM simulator presented by Winterfeld and Wu (2014), whose code is the starting point for this simulator. Normal and shear stresses appearing in those equations are evaluated at the previous timestep, and the rest of the primary variables are evaluated at the current timestep. Solution of those equations yields pressure, mass fractions, temperature, and mean stress at the current timestep. The size of that Jacobian's sub-matrices is two plus the number of mass components. The normal and shear-stress equations, Eqs. 23 to 25 and 27 to 29, are solved next. In those solutions, pressure, mass fractions, temperature, and mean stress are evaluated at the current timestep. Normal and shear stresses appearing in the Laplacian terms are also evaluated at the current timestep, and other instances of those stresses are evaluated at the previous timestep. The Jacobian matrix for each stress-tensor component is linear,

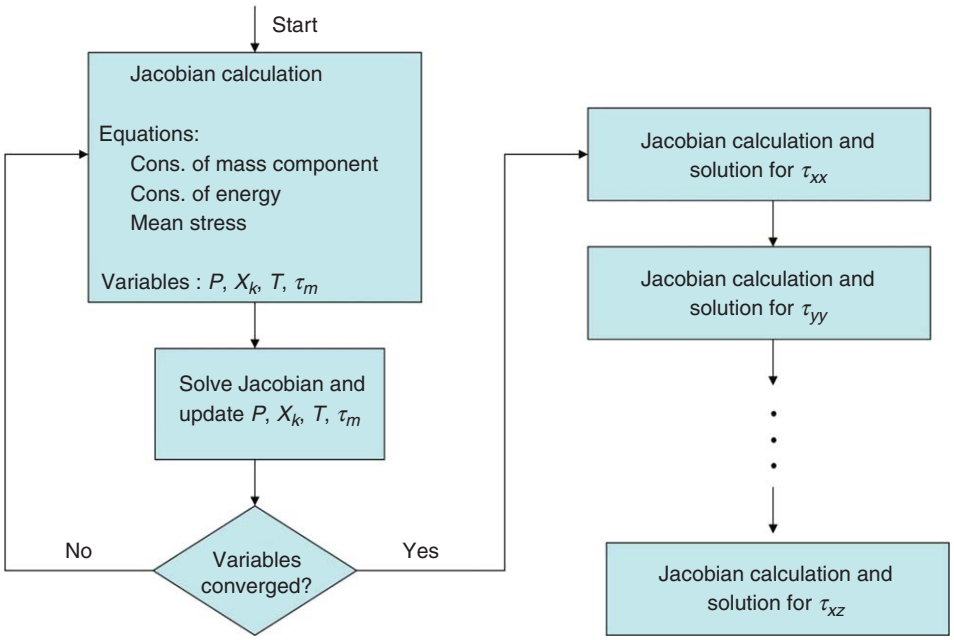

Fig. 1—Flow chart for solution of mass, energy, and geomechanical equations.

independent of the other stress-tensor components, and has a submatrix size of one. The modification of that THM-simulator code to include calculation of these stress-tensor components is relatively straight-forward, and the additional calculations do not increase execution time substantially. **Fig. 1** is a flow chart illustrating this equation solution.

Our simulator is massively parallel, with domain partitioning with the METIS and ParMETIS packages (Karypis and Kumar 1998, 1999). Each processor computes Jacobian-matrix elements for its own gridblocks, and exchange of information between processors uses MPI (message passing interface) and allows calculation of Jacobian-matrix elements associated with interblock connections across domain-partition boundaries. The Jacobian matrix is solved in parallel with an iterative linear solver from the Aztec package (Tuminaro et al. 1999).

Example Problems

We provide four example problems for verification of our technique. The first is a comparison of simulation to the analytical solution for displacement caused by a uniform load on a semi-infinite elastic medium. There is no fluid or heat flow in this problem. The second is a comparison of simulation to the analytical solution for the 2D Mandel-Cryer effect. The last two, a single-phase depletion problem and a simulation of CO_2 injection into a depleting gas reservoir, show a comparison of our simulator to published results.

Displacement From Uniform Load on Semi-Infinite Elastic Medium. With a semi-infinite elastic medium, the displacement caused by a uniform load acting on its surface over a circular area of radius a is given by Timoshenko and Goodier (1951) as

$$w(r) = \frac{4(1-\nu^2)pr}{\pi E}\left(\int_0^{\frac{\pi}{2}}\sqrt{1-\frac{r^2}{a^2}\sin^2\theta}\,\mathrm{d}\theta\right),\ r<a$$

$$w(r) = \frac{4(1-\nu^2)pr}{\pi E} \times\left[\int_0^{\frac{\pi}{2}}\sqrt{1-\frac{a^2}{r^2}\sin^2\theta}\,\mathrm{d}\theta-\left(1-\frac{a^2}{r^2}\right)\int_0^{\frac{\pi}{2}}\frac{\mathrm{d}\theta}{\sqrt{1-\frac{a^2}{r^2}\sin^2\theta}}\right],\ r>a, \quad \ldots\ldots (33)$$

where p is the load, $w(r)$ is displacement at a radius r from the center of the circle, and the integrals in the brackets are elliptic integrals of the first and second kind. The normal z-direction stress along the z-axis at the center of the circle is given as well:

$$\tau_{zz} = p\left[-1+\frac{z^3}{(a^2+z^2)^{\frac{3}{2}}}\right]. \quad \ldots\ldots (34)$$

We used this analytical solution to verify calculation of normal stress-tensor components. We approximated the semi-infinite medium as a large rectangular parallelepiped 194 m in the x- and y- directions and 1320 m in the z-direction. We subdivided this medium into a $200\times200\times800$ Cartesian grid. Gridblock x- and y-direction length in the vicinity of the center was 0.1 m and increased further away from it. Gridblock z-direction length was 0.2 m in the vicinity of the surface and increased further away from it. The loaded circle was at the center of the top xy-face and had a 1.0-m radius. Because our grid was Cartesian, we approximated this circle as 314 loaded squares of radius 0.1 m, as shown in **Fig. 2.** The rest of the medium's surface had no load exerted on it.

Our geomechanical formulation requires boundary conditions for mean stress and those stress-tensor components that are calculated. We specified a mean stress of 0.48 MPa and a normal z-direction stress (the load) of 0.6 MPa over the loaded circle. The equal x- and y-direction normal stresses were then 0.42 MPa. There is no fluid or heat flow in this problem, so only mean stress and stress-tensor components are solved for. We solve for mean stress first, and calculate stress-tensor components next with the mean-stress solution. Because gridblock geometry depends on stress-tensor components that are evaluated at the previous time-step, we must repeat these calculations over a number of time-steps, until the stress-tensor components are converged. This converged solution is that obtained by a fully coupled or fully implicit solution to these stress equations.

The displacement caused by the load is the change of the medium's overall length in the direction of the applied load, given by

$$w = \sum D_{0,z}\varepsilon_{zz}, \quad \ldots\ldots (35)$$

where $D_{0,z}$ is z-direction gridblock unstrained length and the sum is over a z-direction column of gridblocks. The z-direction normal strain is calculated from Hooke's law:

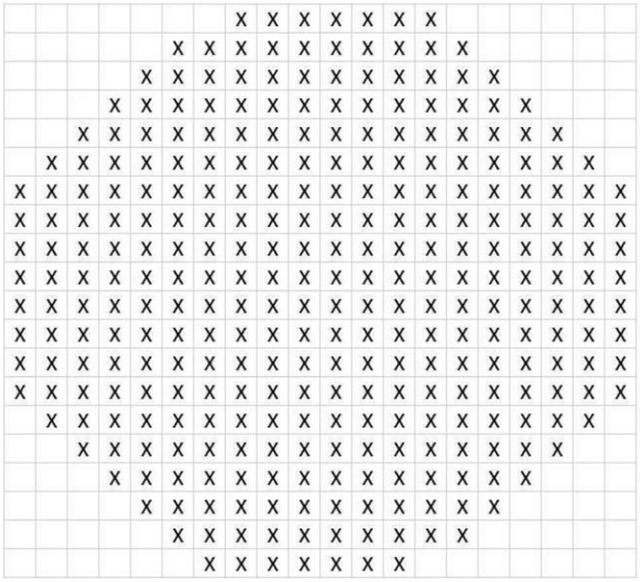

Fig. 2—Approximation of loaded 1.0-m radius circle by 314 square gridblocks of length 0.1 m.

$$\varepsilon_{zz} = \frac{1}{E}[\tau_{zz} - \upsilon(\tau_{xx} + \tau_{yy})]. \quad \ldots\ldots\ldots\ldots\ldots\ldots \quad (36)$$

The analytical and simulated displacements are shown in **Fig. 3,** and those for the z-direction normal stresses are shown in **Fig. 4.** In both cases, they are hardly distinguishable.

The 2D Mandel-Cryer Effect. Consider a fluid-filled poroelastic material with a constant compressive force applied to the top and bottom. There is an instantaneous compression and uniform pore pressure increase caused by the force. Afterward, the material is allowed to drain laterally. Drainage is accompanied by a decrease in pore pressure near the edges, and the material there becomes less stiff, resulting in a load transfer to the center and a pore pressure there that reaches a maximum and then declines. This pore-pressure behavior is the Mandel-Cryer effect (Mandel 1953), and Abousleiman et al. (1996) derived an analytical solution to it. We use this analytical solution to verify our coupled fluid flow and geomechanics calculations.

Our simulation domain is a 1000-m square and is subdivided into a uniform Cartesian 200×200 grid. Rock properties are the following: porosity is 0.094, permeability is 10^{-13} m^2, Young's modulus is 5.0 GPa, Poisson's ratio is 0.25, and Biot's coefficient is 1.0.

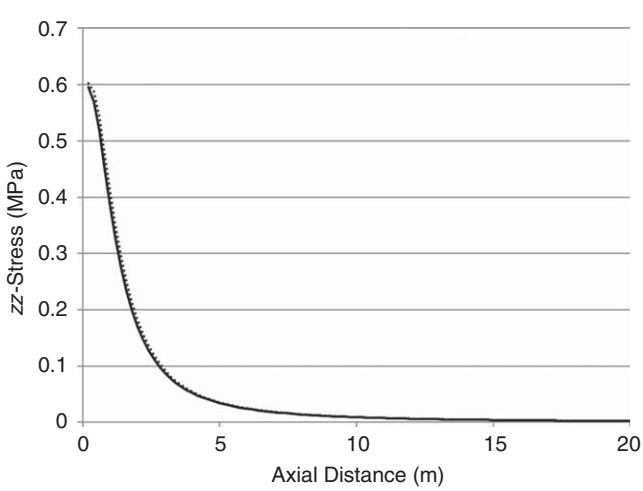

Fig. 4—Analytical (solid line) and simulated (dotted line) z-direction normal stresses for semi-infinite medium subjected to circular load.

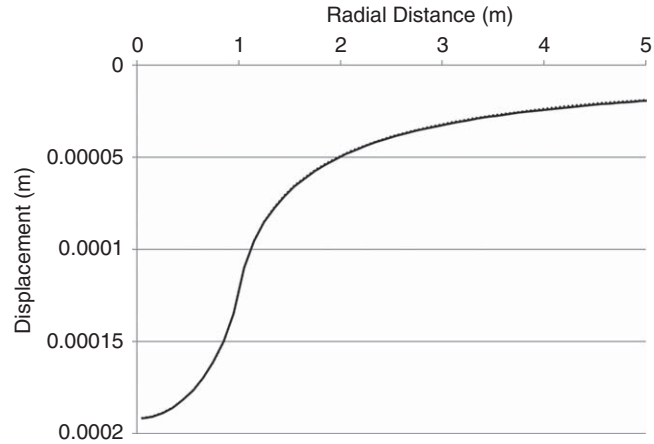

Fig. 3—Analytical (solid line) and simulated (dotted line) displacements for semi-infinite medium subjected to circular load.

We simulate the compression and then the drainage. The initial unstrained state is pore pressure and normal stress components at 2.0 MPa. The compressive portion of the simulation, with an imposed mean stress of 5.0 MPa at the top and bottom, is run until equilibrium is reached. The pore pressure increases to 3.28 MPa in this step, and the mean stress becomes a uniform 5.0 MPa throughout the simulation domain. Because the lateral boundaries are free, the x- and y-direction effective stresses are zero, so the normal stresses in those directions are 3.28 MPa, and the normal z-direction stress is therefore 8.44 MPa.

In the drainage portion of the simulation, the initial pore pressure (2.0 MPa) is imposed at the lateral boundaries. Because the effective stresses there are zero, the x- and y-direction normal stresses there have that value. The normal z-direction stresses at the top and bottom remain at 8.44 MPa. The drainage simulation is run for 100,000 seconds with 100-second timesteps. **Fig. 5** shows the match of centerline pore pressure with the analytical solution. The displacements in the x- and z-direction are calculated as was performed in the previous example problem. The applied stress causes the system to contract in the z-direction and expand in the x-direction. The expansion, shown in **Fig. 6,** is matched almost perfectly, and the match of the contraction, shown in **Fig. 7,** shows only a small deviation from the analytical solution at early times.

Depletion of a Single-Phase Reservoir. We ran the depletion of a single-phase reservoir, adapted from Dean et al. (2006), as a comparison of our simulator to published results. A single-phase (water) reservoir, 671 m^2 in area and 61 m thick, with a single vertical well at the center and completed along the entire thickness, was produced at a constant rate of 27.59 kg/s for 500 days. Reservoir porosity was initially 0.20, horizontal permeability was $5{\cdot}10^{-14}$ m^2, vertical permeability was $5{\cdot}10^{-15}$ m^2, Young's modulus was $6.87{\cdot}10^7$ Pa, Poisson's ratio was 0.30, and the rock density was 2700 kg/m^3. The z-direction stress at the reservoir top was 41.4 MPa, and the constant horizontal stresses were 27.6 MPa. Pore pressure at the reservoir top was 20.7 MPa. Pore pressure increased with increasing depth caused by the hydrostatic gradient, and z-direction stress increased with increasing depth caused by the overburden.

Our Cartesian grid was $11 \times 11 \times 10$ with constant gridblock dimensions, and our timestep size was 50 days. We used the same relations for porosity and gridblock volume as used by Dean et al. (2006); gridblock volume was constant, and porosity varied with volumetric strain as

$$\phi = \phi_i + \varepsilon_{v,i} - \varepsilon_v, \quad \ldots\ldots\ldots\ldots\ldots\ldots\ldots\ldots \quad (37)$$

where subscript i refers to initial conditions.

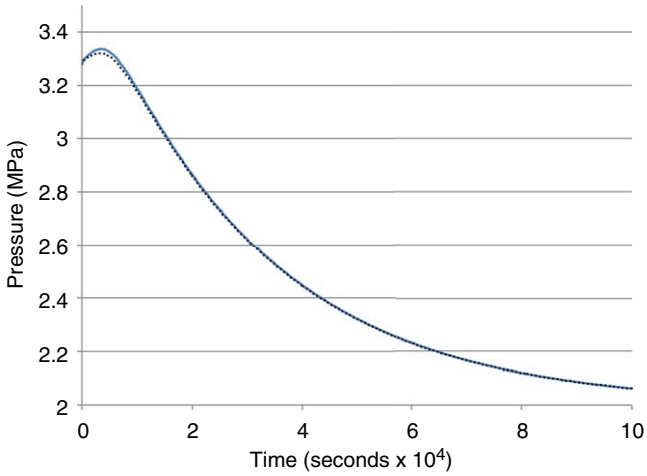

Fig. 5—Match of simulated centerline pore pressure (dotted line) with analytical solution (solid line) for Mandel-Cryer effect.

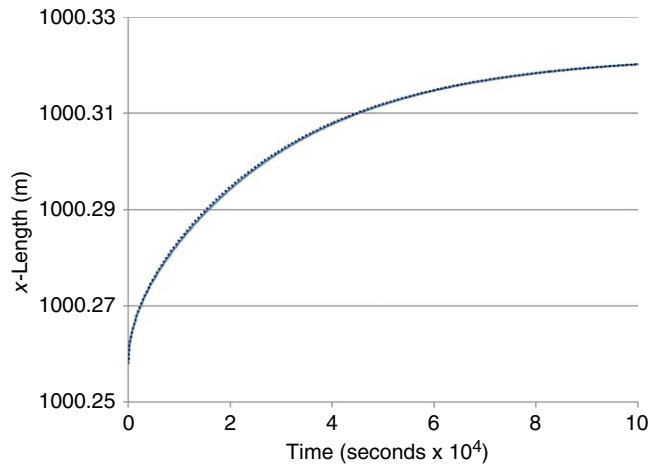

Fig. 6—Match of simulated *x*-direction displacement (dotted line) with analytical solution (solid line) for Mandel-Cryer effect.

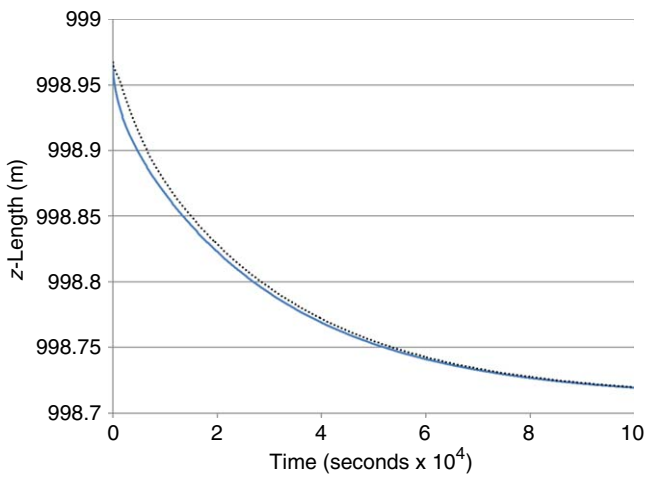

Fig. 7—Match of simulated *z*-direction displacement (dotted line) with analytical solution (solid line) for Mandel-Cryer effect.

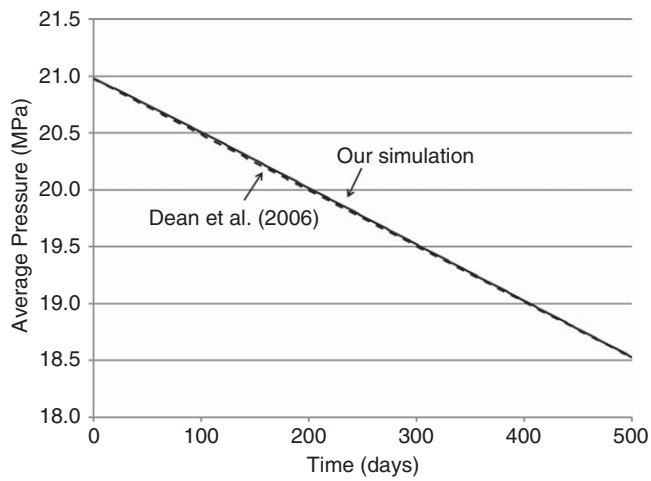

Fig. 8—Average pore pressure from our simulation compared with Dean et al. (2006).

Fig. 8 shows a comparison of average reservoir pressure, and **Fig. 9** shows a comparison of subsidence around the well, between our simulation and Dean et al. (2006). The average-reservoir-pressure match necessitated usage of the previous-gridblock volume and porosity relations and would not be as good if gridblock volume varied with volumetric strain and porosity varied with effective stress, as we formulated previously. Our subsidence is very similar to the published results and differs by approximately 5% at 500 days.

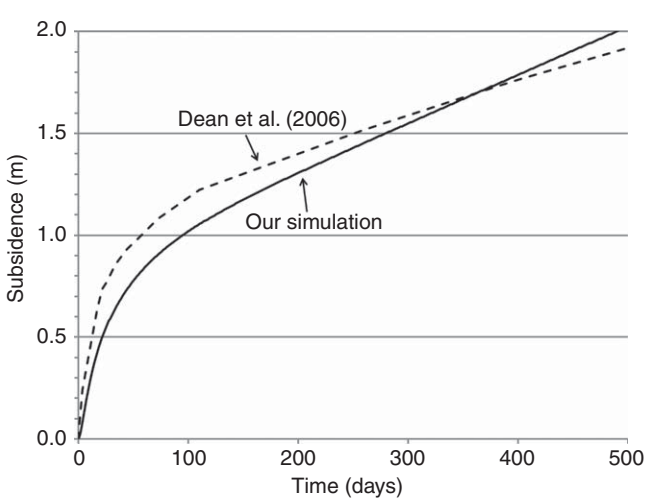

Fig. 9—Subsidence from our simulation compared with Dean et al. (2006).

In Salah Gas Project. The In Salah Gas Project, in central Algeria, is a CO_2-storage project. Natural gas produced nearby is high in CO_2, and this CO_2 is injected back into the water leg of a depleting gas field for geological storage. Surface uplift from CO_2 injection was measured by satellite-based inferrometry, and Rutqvist et al. (2010) performed a reservoir-geomechanical analysis of In Salah CO_2 injection and surface uplift with the TOUGH2-FLAC numerical simulator (Rutqvist et al. 2002) to determine whether the uplift can be explained by pressure changes and deformation in the injection zone only. We reran their analysis on our simulator to match their simulated results.

The domain was $10\times10\times4$ km with one 1.5-km horizontal injection well at 1810-m depth and in the domain center. The domain consisted of four geological layers—Shallow Overburden, Caprock, Injection Zone, and Base; their properties are shown in **Table 2.** The reservoir initially contained water at hydrostatic equilibrium. The initial temperature and pressure at the injection well were 90 °C and 18.5 MPa, respectively. The initial stress tensor was calculated assuming no shear stresses. Then, the normal z-direction stress, from Eq. 14, satisfies

$$\frac{\partial \tau_{zz}}{\partial z} + F_{b,z} = 0. \quad \ldots\ldots\ldots\ldots\ldots\ldots\ldots\ldots \quad (38)$$

Property	Shallow Overburden (0–900 m)	Caprock (900–1800 m)	Injection Zone (1800–1820 m)	Base (>1800 m)
Young's modulus (GPa)	1.5	20.0	6.0	20.0
Poisson's ratio	0.2	0.15	0.2	0.15
Biot's coefficient	1.0	1.0	1.0	1.0
Porosity	0.1	0.01	0.17	0.01
Permeability (m^2)	1.0×10^{-17}	1.0×10^{-19}	0.875×10^{-14}	1.0×10^{-21}
Residual CO_2 saturation	0.05	0.05	0.05	0.05
Residual liquid saturation	0.3	0.3	0.3	0.3
Van Genuchten (1980) (m)	0.457	0.457	0.457	0.457
Van Genuchten, P_0 (kPa)	19.9	621.0	19.9	621.0

Table 2—Geological-layer properties for In Salah CO_2 injection.

Normal stresses are also assumed to have only z-direction dependence. Then, Eqs. 23 and 24 become

$$\frac{\partial^2}{\partial z^2}\left\{\tau_{xx} - h(\mathbf{P},\mathbf{T}) - \frac{3\upsilon}{1+\upsilon}[\tau_m - h(\mathbf{P},\mathbf{T})]\right\} = 0 \quad \ldots\ldots (39)$$

and

$$\frac{\partial^2}{\partial z^2}\left\{\tau_{yy} - h(\mathbf{P},\mathbf{T}) - \frac{3\upsilon}{1+\upsilon}[\tau_m - h(\mathbf{P},\mathbf{T})]\right\} = 0. \quad \ldots\ldots (40)$$

At a reference elevation, z_0, we specify normal stress-tensor components and two normal stress ratios, R_{xz} and R_{yz}, given by

$$\lim_{z\to z_0}\frac{\tau_{xx} - \tau_{xx,0}}{\tau_{zz} - \tau_{zz,0}} = R_{xz} \quad \ldots\ldots (41)$$

and

$$\lim_{z\to z_0}\frac{\tau_{yy} - \tau_{yy,0}}{\tau_{zz} - \tau_{zz,0}} = R_{yz} \quad \ldots\ldots (42)$$

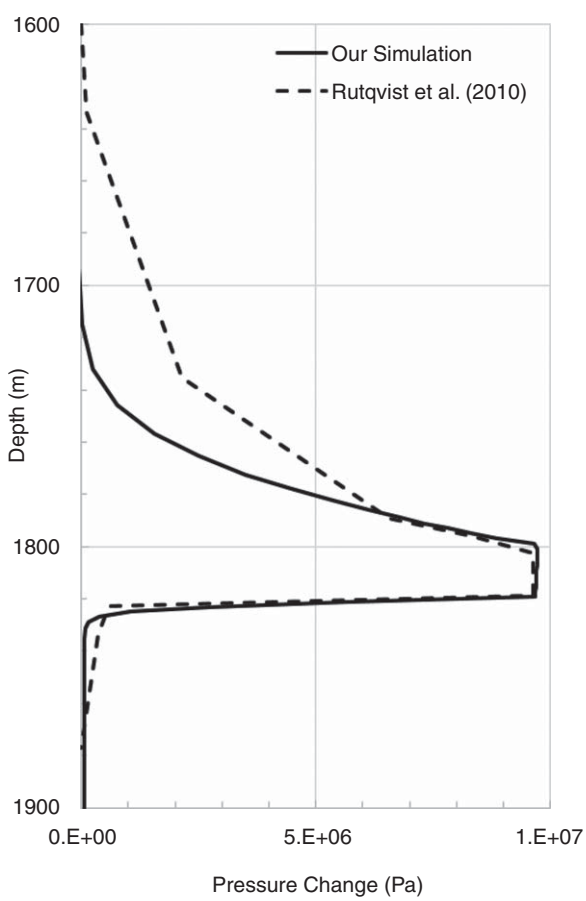

Fig. 10—Pressure change at injection-well center after 3 years of injection.

to completely determine the normal stress-tensor components. These ratios were 1.2 and 0.8, respectively. The lateral reservoir boundaries were maintained at constant pressure, the reservoir boundaries were maintained at constant stress, and CO_2 was injected at $9.734\,\mathrm{kg\cdot sec^{-1}}$ for 3 years. Surface uplift results from changes in gridblock height, which is given by

$$\Delta z_k = \Delta z_{k,i}\frac{(1-\varepsilon_{zz})}{(1-\varepsilon_{zz,i})}, \quad \ldots\ldots (43)$$

where ε_{zz} is the z-direction normal strain and subscript i refers to initial conditions.

Our simulation was over a 5×5×4-km quarter-symmetry element of the domain with a 50×50×60 grid. In all three directions, the grid was finer in the vicinity of the well and became coarser away from it. **Fig. 10** compares pressure change vs. depth. We modified the Rutqvist et al. (2010) injection-zone permeability somewhat to match the pressure change there after 3 years. Their simulation used a much coarser grid than ours (approximately 10,000 gridblocks for the entire domain) and is reflected by their piecewise-linear pressure profile. **Fig. 11** compares vertical displacement vs. depth at the injection-well center after 3 years. Both simulators give similar displacement profiles.

Summary and Conclusions

We developed a reservoir simulator for modeling THM processes in fractured and porous media. The simulator geomechanical formulation consists of a momentum-conservation equation for mean stress, pore pressures, and temperatures, along with additional equations relating each stress-tensor component to mean stress, pore pressures, and temperatures. The fluid- and heat-flow formulation is for general multiphase, multicomponent, multiporosity systems. The simulator is an extension of a THM one with geomechanical formulation that was the momentum-conservation equation for mean stress alone.

We verified our technique with analytical solutions and published results. For the analytical solutions, we matched the displacement from a uniform load on semi-infinite elastic medium and the 2D Mandel-Cryer effect. Both analytical solutions were matched by simulation extremely well, verifying the technique for calculating stress-tensor components. We also ran simulations, published in the literature, of single-phase depletion of a reservoir and CO_2 injection into a depleting gas field. The results from our simulation, namely pressures and displacements, agreed well with the published results.

Nomenclature

a = radius, m
A = area, L^2, m^2
C = specific heat, L^2/t^2T, J/kg·K
D = distance, L, m
$\boldsymbol{F}$ = mass flux, m/L^2t, $kg/m^2\cdot s$
$\boldsymbol{F}_{\mathbf{adv}}$ = advective mass flux, m/L^2t, $kg/m^2\cdot s$
$\boldsymbol{F}_{\mathbf{b}}$ = body force, cm^3/t^2, $kg\cdot m/s^2$
$\boldsymbol{g}$ = gravity vector, L/t^2, m/s^2

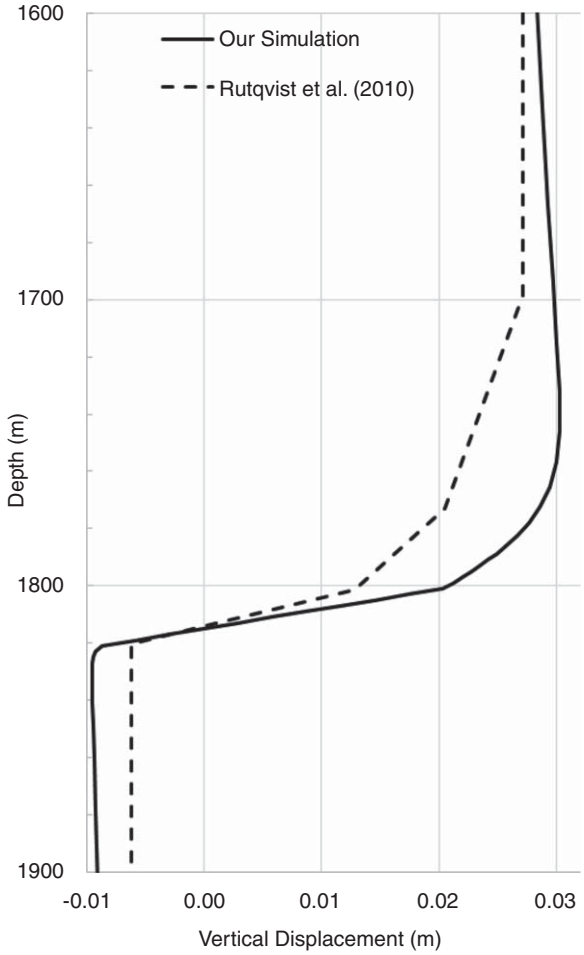

Fig. 11—Vertical displacement at injection well center after 3 years of injection.

G = shear modulus, m/Lt^2, Pa
h = specific enthalpy, L^2/t^2, J/kg
$\boldsymbol{I}$ = identity matrix
k = permeability, L^2, m^2
k_r = relative permeability
k_t = thermal conductivity, cm^3/t^{3}T, J/m·s·K
K = bulk modulus, m/Lt^2, Pa
K_s = solid modulus, m/Lt^2, Pa
K_* = solid modulus without fractures, m/Lt^2, Pa
M^k = conserved species per unit volume, m/L^3, kg/m^3 or m/Lt^2, J/m^3
N = number of mass components
p = load, m/Lt^2, Pa
P = pressure, m/Lt^2, Pa
P_c = capillary pressure, m/Lt^2, Pa
q = mass source/sink per unit volume, m/L^{3}t, kg/m^3·s
S = saturation
t = time, t, seconds
T = temperature, T, K
T_{ref} = reference temperature, T, K
$\boldsymbol{u}$ = displacement vector, L, m
U = specific internal energy, L^2/t^2, J/kg
V = bulk volume, L^3, m^3
V_s = solid volume, L^3, m^3
w = displacement, m
X = mass fraction
α = Biot's coefficient
β = linear thermal-expansion coefficient, 1/T, 1/K
$\boldsymbol{\varepsilon}$ = strain tensor
ε_v = volumetric strain
λ = Lamé parameter, m/Lt^2, Pa
μ = viscosity, m/Lt, Pa·s
ν = Poisson's ratio
ρ = density, m/L^3, kg/m^3
$\boldsymbol{\tau}$ = stress tensor, m/Lt^2, Pa
τ_m = mean stress, m/Lt^2, Pa
τ' = effective stress, m/Lt^2, Pa
ϕ = porosity
ω = volume fraction

Subscripts
l = phase
r = rock
0 = unstrained

Superscripts
i = initial
k = conserved species
n = timestep

Acknowledgments

This work was supported by Foundation CMG, by the Energy Modeling Group of the Colorado School of Mines, and by the National Energy Technology Laboratory of the US Department of Energy.

References

Abousleiman, Y., Cheng, A. H.-D., Cui, L. et al. 1996. Mandel's Problem Revisited. *Géotechnique* **46** (2): 187–195. http://dx.doi.org/10.1680/geot.1996.46.2.187.

Bai, M., Elsworth, D., and Roegiers, J.-C. 1993. Modeling of Naturally Fractured Reservoirs Using Deformation Dependent Flow Mechanism. *Int. J. Rock Mech. Min. Sci. and Geomech. Abstr.* **30** (7): 1185–1191. http://dx.doi.org/10.1016/0148-9062(93)90092-R.

Biot, M. A. and Willis, D. G. 1957. The Elastic Coefficients of the Theory of Consolidation. *J. Appl. Mech.* **24:** 594–601.

Chin, L. Y., Raghavan, R., and Thomas, L. K. 2000. Fully Coupled Geomechanics and Fluid-flow Analysis of Wells With Stress-dependent Permeability. *SPE J.* **5** (1): 32–45. SPE-58968-PA. http://dx.doi.org/10.2118/58968-PA.

Chin, L. Y., Thomas, L. K., Sylte, J. E. et al. 2002. Iterative Coupled Analysis of Geomechanics and Fluid Flow for Rock Compaction in Reservoir Simulation. *Oil and Gas Science and Technology* **57** (5): 485–497. http://dx.doi.org/10.2516/ogst:2002032.

Dean, R. H., Gai, X., Stone, C. M. et al. 2006. A Comparison of Techniques for Coupling Porous Flow and Geomechanics. *SPE J.* **11** (1): 132–140. SPE-79709-PA. http://dx.doi.org/10.2118/79709-PA.

Gutierrez, M. and Lewis, R. W. 1998. The Role of Geomechanics in Reservoir Simulation. Presented at the SPE/ISRM Eurock'96, Trondheim, Norway, 8–10 July. SPE-47392-MS. http://dx.doi.org/10.2118/47392-MS.

Hu, L., Winterfeld, P. H., Fakcharoenphol, P. et al. 2013. A Novel Fully-coupled Flow and Geomechanics Model in Enhanced Geothermal Reservoirs. *Journal of Petroleum Science and Engineering* **107:** 1–11. http://dx.doi.org/10.1016/j.petrol.2013.04.005.

Jaeger, J. C., Cook, N. G. W., and Zimmerman, R. W. 2007. *Fundamentals of Rock Mechanics*. Malden, Massachusetts, USA: Blackwell Publishing.

Karypis, G. and Kumar, V. 1998. A Parallel Algorithm for Multilevel Graph Partitioning and Sparse Matrix Ordering. *Journal of Parallel and Distributed Computing* **48:** 71–95. http://dx.doi.org/10.1006/jpdc.1997.1403.

Karypis, G. and Kumar, V. 1999. A Fast and High Quality Multilevel Scheme for Partitioning Irregular Graphs. *Siam J. Sci. Comput.* **20** (1): 359–392. http://dx.doi.org/10.1137/S1064827595287997.

Mandel, J. 1953. Consolidation des sols (Étude mathématique). *Géotechnique* **3** (7): 287–299. http://dx.doi.org/10.1680/goet.1953.3.7.287.

McTigue, D. F. 1986. Thermoelastic Response of Fluid-saturated Porous Rock. *Journal of Geophysical Research* **91** (B9): 9533–9542. http://dx.doi.org/10.1029/JB091iB09p09533.

Minkoff, S. E., Stone, C. M., Arguello, J. G. et al. 1999. Staggered in Time Coupling of Reservoir Flow Simulation and Geomechanical Deformation: Step 1—One-way Coupling. Presented at the SPE

Reservoir Simulation Symposium, Houston, 14–17 February. SPE-51920-MS. http://dx.doi.org/10.2118/51920-MS.

Narasimhan, T. N. and Witherspoon, P. A. 1976. An Integrated Finite Difference Method for Analysis of Fluid Flow in Porous Media. *Water Resources Res.* **12:** 57–64. http://dx.doi.org/10.1029/WR012i001p00057.

Pruess, K., Oldenburg, C., and Moridis, G. 1999. *TOUGH2 User's Guide*, Version 2.0. Report LBNL-43134, Lawrence Berkeley National Laboratory, Berkeley, California.

Rutqvist, J. and Tsang, C.-F. 2002. A Study of Caprock Hydromechanical Changes Associated With CO_2 Injection Into a Brine Aquifer. *Environ. Geol.* **42:** 296–305. http://dx.doi.org/10.1007/s00254-001-0499-2.

Rutqvist, J., Wu, Y.-S., Tsang, C.-F. et al. 2002. Modeling Approach for Analysis of Coupled Multiphase Fluid Flow, Heat Transfer, and Deformation in Fractured Porous Rock. *Int. J. Rock Mech. and Min. Sci.* **39:** 429–442. http://dx.doi.org/10.1016/S1365-1609(02)00022-9.

Rutqvist, J., Vasco, D. W. and Myer, L. 2010. Coupled Reservoir-Geomechanical Analysis of CO_2 Injection and Ground Deformations at In Salah, Algeria. *Int. J. of Greenhouse Gas Control* **4:** 225–230. http://dx.doi.org/10.1016/j.ijggc.2009.10.017.

Settari, A. and Mourits, F. M. 1998. A Coupled Reservoir and Geomechanical Simulation System. *SPE J.* **3** (3): 219–226. SPE-50939-PA. http://dx.doi.org/10.2118/50939-PA.

Settari, A. and Walters, D. A. 1999. Advances in Coupled Geomechanical and Reservoir Modeling With Applications to Reservoir Compaction. Presented at the SPE Reservoir Simulation Symposium, Houston, 14–17 February. SPE-51927-MS. http://dx.doi.org/10.2118/51927-MS.

Timoshenko, S. and Goodier, J. N. 1951. *Theory of Elasticity*. New York, New York: McGraw-Hill Book Company, Inc.

Tran, D., Nghiem, L., and Buchanan, L. 2005. Improved Iterative Coupling of Geomechanics With Reservoir Simulation. Presented at the SPE Reservoir Simulation Symposium, Houston, 31 January–5 February. SPE-93244-MS. http://dx.doi.org/10.2118/93244-MS.

Tuminaro, R. S., Heroux, M., Hutchinson, S. A. et al. 1999. *Official Aztec User's Guide*, Version 2.1. Massively Parallel Computing Research Laboratory, Sandia National Laboratories, Albuquerque, New Mexico, USA.

van Genuchten, M.Th. 1980. A Closed-Form Equation for Predicting the Hydraulic Conductivity of Unsaturated Soils. *Soil Sci. Soc* **44** (5): 892–898.

Wan, J., Durlofsky, L. J., Hughes, T. J. R. et al. 2003. Stabilized Finite Element Methods for Coupled Geomechanics-Reservoir Flow Simulations. *Proc.,* SPE Reservoir Simulation Symposium, Houston, 3–5 February. SPE-79694-MS. http://dx.doi.org/10.2118/79694-MS.

Wilson, R. K. and Aifantis, E. C. 1982. On the Theory of Consolidation With Double Porosity. *Int. J. Eng. Sci.* **20** (9): 1009–1035. http://dx.doi.org/10.1016/0020-7225(82)90036-2.

Winterfeld, P. H. and Wu, Y.-S. 2014. Simulation of CO_2 Sequestration in Brine Aquifers With Geomechanical Coupling. In *Computational Models for CO_2 Sequestration and Compressed Air Energy Storage*, ed. J. Bundschuh and R. Al-Khoury, Chap. 8, pp. 275–303, New York, New York: CRC Press.

Xiong, Y., Fakcharoenphol, P., Winterfeld, P. et al. 2013. Coupled Geomechanical and Reactive Geochemical Model for Fluid and Heat Flow: Application for Enhanced Geothermal Reservoir. Presented at the SPE Reservoir Characterization and Simulation Conference and Exhibition, Abu Dhabi, 16–18 September. SPE-165982-MS. http://dx.doi.org/10.2118/165982-MS.

Philip H. Winterfeld is Research Associate Professor in the Petroleum Engineering Department at the Colorado School of Mines. His current research interests include numerical simulation and flow and transport in porous media, including coupled processes of fluid flow and rock deformation. Winterfeld holds a BS degree from Massachusetts Institute of Technology and a PhD degree from the University of Minnesota, both in chemical engineering.

Yu-Shu Wu is a professor in petroleum engineering, Foundation CMG Reservoir Modeling Chair, and Director of the EMG research center in the Department of Petroleum Engineering, Colorado School of Mines. He is a Fellow of Geological Society of America and recipient in 2015 of SPE Distinguished Membership. Wu is also a guest scientist at the Earth Sciences Division of the Lawrence Berkeley National Laboratory. He earned undergraduate and MS degrees in petroleum engineering in China, and MS and PhD degrees in reservoir engineering from the University of California at Berkeley. During his career, Wu has authored or coauthored numerous journal and conference papers, reports, and book chapters, including 100+peer-reviewed journal papers and 16 peer-reviewed book chapters as well as 50+SPE papers.